Supplementary Information (SI) for Analytical Methods.
This journal is © The Royal Society of Chemistry 2026

Supporting information

Eco-Benign S-Doped g-C_3N_4 Nano-Architectonics for Rapid and Selective Fluorescent Detection of the Jaundice Biomarker .

Govindha Pandi Rajaram [a, b], *Murugan Veerapandian* [a, b*], *Shanmugam Senthilkumar* [a, b*]

[a] *Electrodics and Electrocatalysis Division, CSIR-Central Electrochemical Research Institute (CECRI), Karaikudi 630 003, Tamil Nadu, India.*

[b] *Academy of Scientific and Innovative Research (AcSIR), Ghaziabad 201002, India.*

**Corresponding Author*

Email: ssenthilmugam@gmail.com ; ssenthilkumar@cecri.res.in ; vmurugan.cecri@csir.res.in

Content

Section 1 . synthesis of artificial urine , stock solution of analyte and florescent probe

To create artificial urine (AU) that mimics physiological human urine, the method described in the previous work[1] was followed. The preparation involved dissolving specific quantities of various compounds in 1000 milliliters of deionized water. The components included 1.7 grams of sodium sulfate, 0.25 grams of urea, 0.72 grams of sodium citrate dehydrate, 0.881 grams of creatinine, 15 grams of urea, 2.308 grams of potassium chloride, 0.185 grams of calcium chloride, 1.26 grams of ammonium chloride, 0.035 grams of potassium oxalate monohydrate, 1.08 grams of magnesium sulfate heptahydrate, 0.83 grams of disodium hydrogen phosphate, and 2.912 grams of sodium dihydrogen phosphate. This mixture was considered as the stock artificial urine for subsequent analysis.

The stock solutions of BIL were prepared by taking 0.58466 g BIL, adding 100 µL of 1 M NaOH to dissolve, and making up to 10 mL by adding distilled water. Similarly, the stock solutions of the fluorescent probe were prepared by taking 1 mg of S-g-C_3N_4 and dispersing it into 5 ml of 0.1 M PBS (pH = 7.4), in order to achieve proper dispersion of S-g-C_3N_4 colloidal solution treating 10 mints with ultra-sonication. The sensitivity was investigated by successively adding a known concentration of BIL to the S-g-C_3N_4 fluorescent probe.

Section 2. Material characterisation

S1. Elemental composition of S-g-C_3N_4:

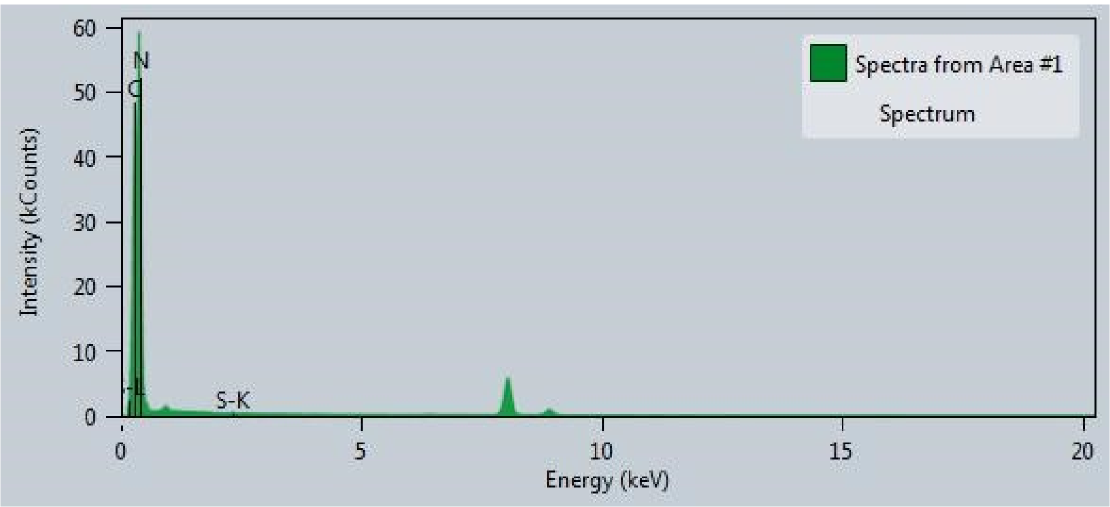

Figure S1.*Elemental composition of S-g-C_3N_4*

S2. X-ray photon spectroscopy (XPS) of S-g-C_3N_4.

The elemental bonding arrangement and surface chemical compositions are further investigated by High Resolution X-ray photoelectron spectroscopy (HR-XPS) investigations. The presence of the C, N, S, and O elements in S-g-C_3N_4 is suggested by the full XPS survey spectrum shown in **Figure 2a**; the corresponding element contents are 43.89 at%, 52.49 at%, 0.53 at%, and 3.09 at%, respectively. The successful doping of S species into g-C_3N_4 moiety is demonstrated by the clearly distinctive peaks of S2p, which are located at about 162.22 eV. The C1s XPS spectra (**Figure 2b**) of depict the chemical environment of carbon in the material. A strong intensity peak at 284.7 eV, linked to sp^2 hybridized carbon atoms, indicates the presence of aromatic rings and adds to the material's electrical properties. The moderately sharp peak at 281.61 eV, which emphasizes the carbon framework's conjugated system, displays the structural integrity of the structure. There is minimal surface functionalization or oxidation, as indicated by the low-intensity peak at 290.465 eV. Sulfur doping enhanced surface area and active edge sites, improving sp^2 carbon visibility. Similarly, the N1s XPS spectrum of g-C_3N_4 reveals that the presence of the nitrogen coordination and bonding states in S-g-C_3N_4 **(Figure 2c).** As nitrogen atoms bound to carbon in a graphitic configuration, the high intensity peak at 397.23 eV usually represents the nitrogen in the triazine (or) heptazine ring structure of g-C_3N_4. In a similar vein, a moderately intense peak at 398.65 eV would suggest that nitrogen is in a different bonding environment, perhaps connected to three carbon atoms (N-C3). The amino group in g-C_3N_4 is also responsible for the peak at 402.68 eV. The low intense peak at 404.75 eV is related to more oxidized nitrogen species, such as nitro groups (-NO_2) or other nitrogen species associated with surface oxidation) .**Figure 2(e)** shows the high-resolution S2p spectrum of S-g-C_3N_4. The clear peaks centered at 162.22 eV imply the presence of a C-S-C bond in S-g-C_3N_4 confirming the successful integration of S atoms into g-C_3N_4. Furthermore, the oxidized sulfur SO_4^{2-} species is responsible for the remaining distinct peaks seen at 166.22 eV, confirming the presence of surface oxidation brought on by air contact. The high-resolution O 1s spectra of S-g-C_3N_4 is shown in **Figure 2d**. The HO-C = O bond, which primarily comes from the adsorption of H_2O or CO_2 on the catalyst surface, has a binding energy of 532.5 eV [2] (Spectrum was provided in main manuscript).

Element	**Atomic %**
S 2s	**0.53**
C 1s	**43.89**
N 1s	**52.49**
O 1s	**3.09**

Figure S2.*Atomic weight percentage of sulfur, carbon, nitrogen, and oxygen presents in the S-g-C_3N_4*

Section 3. Sensing of BIL

S3. Self-quenching effect of BIL:

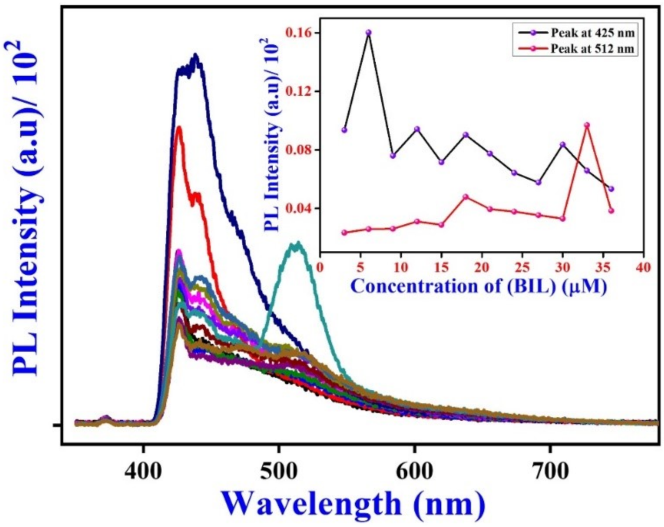

Figure S3.*PL spectrum of continuous addition of known concentration of bare BIL in 0.1 M PBS at pH =7.4) upon excitation wavelength of 370 nm. (Spectrum recorded at 5 nm slit and 400 V photovoltage is applied)*

S4. UV Visible and PL Spectrum of S- g-C_3N_4 and BIL:

In PL Spectrum, when S- g-C_3N_4 is excited at 370 nm, a blue fluorescence with an emission peak centred at 450 nm is produced .The excitation-independent and pH -dependent emission is noted in S- g-C_3N_4 due to the presence of multiple emissive centres within the material. Sulfur doping introduces new defect sites and alters the electronic structure of g-C_3N_4. These sulfur-related defects act as additional emissive centers that can trap and re-emit light over a broad range of energies. Since these centers have relatively similar energy gaps, they tend to exhibit fluorescence that is independent of the excitation wavelength. The excitation independence arises because the recombination of charge carriers (electrons and holes) occurs at these sulfur-induced mid-gap states rather than at the intrinsic conduction and valence bands of pure g-C_3N_4. Sulfur doping introduces heterogeneity in the energy landscape of g-C_3N_4. The different emissive sites can cover a range of energy levels, allowing emission to occur over a wide range of wavelengths regardless of the excitation energy. This makes the emission excitation-independent, as the excited electrons have various paths to recombine and emit photons. The defects introduced by sulfur may serve as photon-trapping centers that slow down the recombination dynamics of electron-hole pairs, making the emission process less dependent on the exact energy of the excitation photons.

BIL exhibits three notable absorption peaks at 268 nm, 325 nm, and 370 nm **Figure S4a.** Each of these peaks corresponds to different electronic transitions associated with the BIL molecule. The peak at 268 nm is typically attributed to $\pi \rightarrow \pi^*$ transitions in the conjugated double bond system of the BIL structure. It reflects the presence of conjugated systems, where electrons are excited from a bonding π orbital to an anti-bonding π* orbital. The peak at 325 nm is also associated with π → π* transitions, but may involve different configuration or conformations of the molecule, potentially influenced by solvent effects or intermolecular interactions. Similarly, a broad peak at 370 nm suggests the involvement of both π → π* transitions and possibly n →π* transitions. The broad nature indicates that there may be multiple overlapping electronic transitions occurring in this region.

When BIL is excited at 370 nm, a weak yellowish-green fluorescence with multiple emission peaks centered at 440 nm (with moderate intensity),520nm (with high intensity and peak maxima), and 655 nm with very low intensity is noted in **Figure S4b.** BIL exhibits excitation-dependent and pH-dependent PL, which arises due to a combination of multiple electronic transitions within its conjugated structure, flexible conformations, self-absorption effects, and aggregation in solution. It suggests that this behaviour reflects the unique photophysical properties of BIL and contributes to its complex spectral profile.

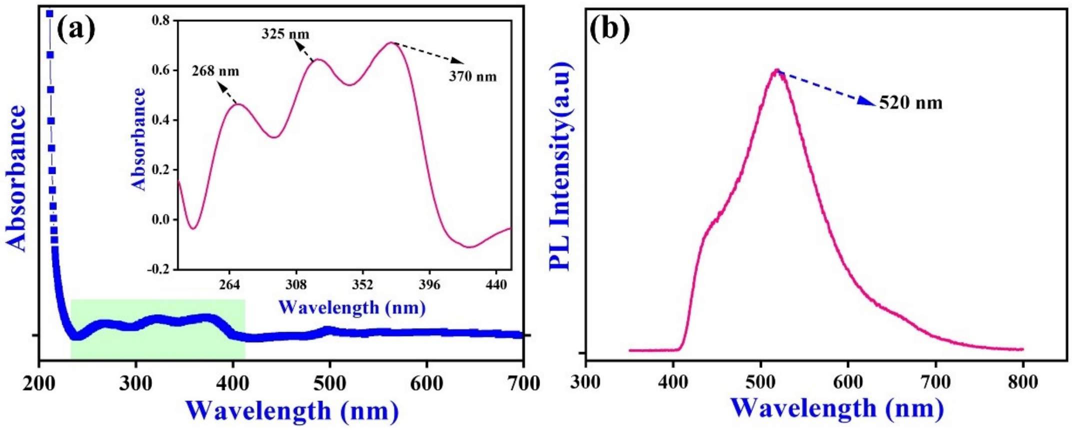

Figure S4. *(a) baseline corrected UV-spectrum profile of BIL in 0.1 M PBS (pH = 7.4); (b) emission spectra of BIL in 0.1 M PBS (pH = 7.4) upon excitation wavelength of 370 nm. (Spectrum recorded at 5 nm slit and 400 V photovoltage is applied).*

S5. Comparison of excitation and emission Spectrum of S- g-C_3N_4 (Stoke shift):

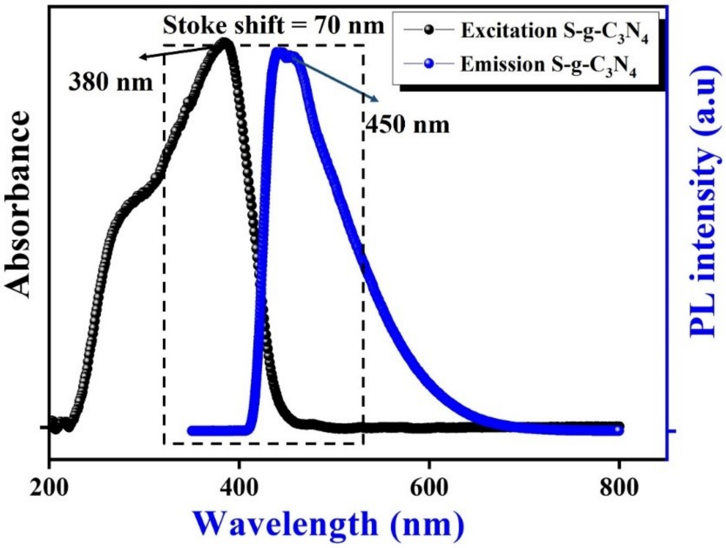

Figure S5. *comparison of baseline corrected excitation and emission spectrum of S-g-C_3N_4 in 0.1 M PBS (pH = 7.4).*

S6.BIL sensing:

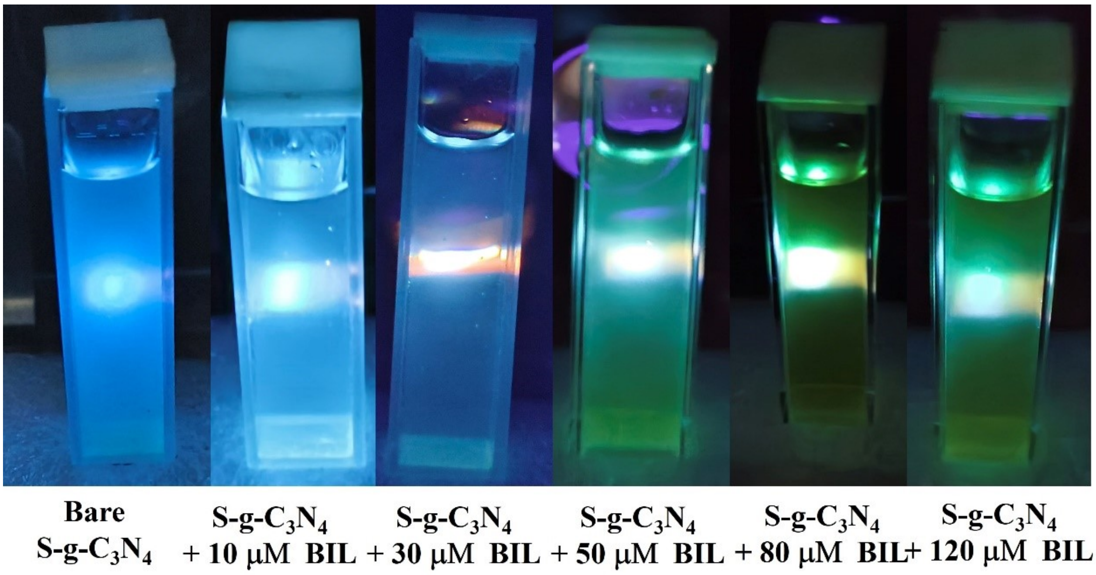

Figure S6. *Real photograph of Fluorescence images of S-g-C_3N_4 with various known concentration of BIL.*

S7.Human finger print on various substrate :

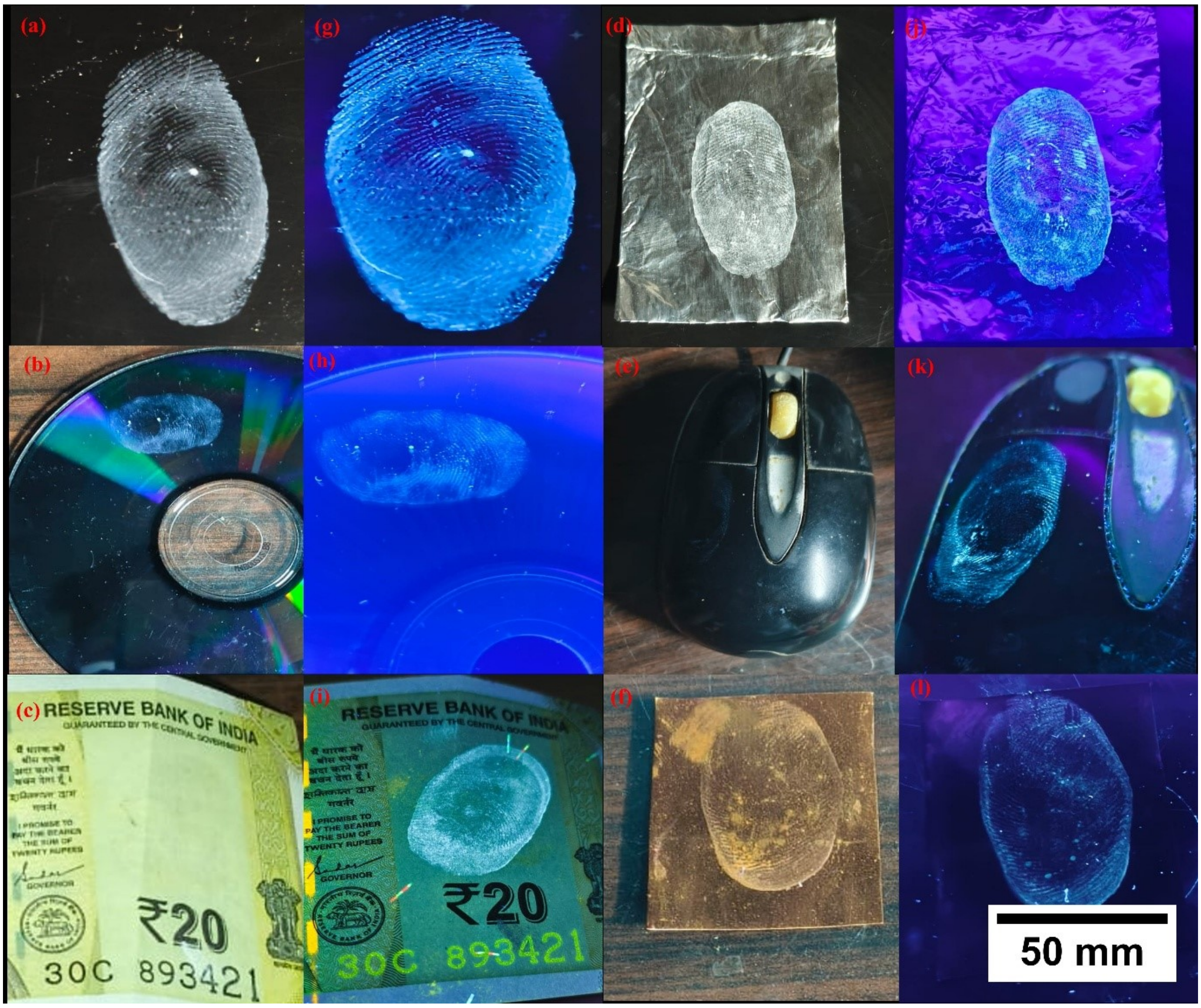

Figure S7. *real photograph of Finger print images on various substrate like (a) plastic table,(b)CD ,(c) currency note, (d)aluminium foil ,(e)mouse, (f) Copper plate. (g to l) represent their fluorescence image under UV Light .*

S8.CIE Diagram of S-g-C_3N_4 before and after addition with BIL:

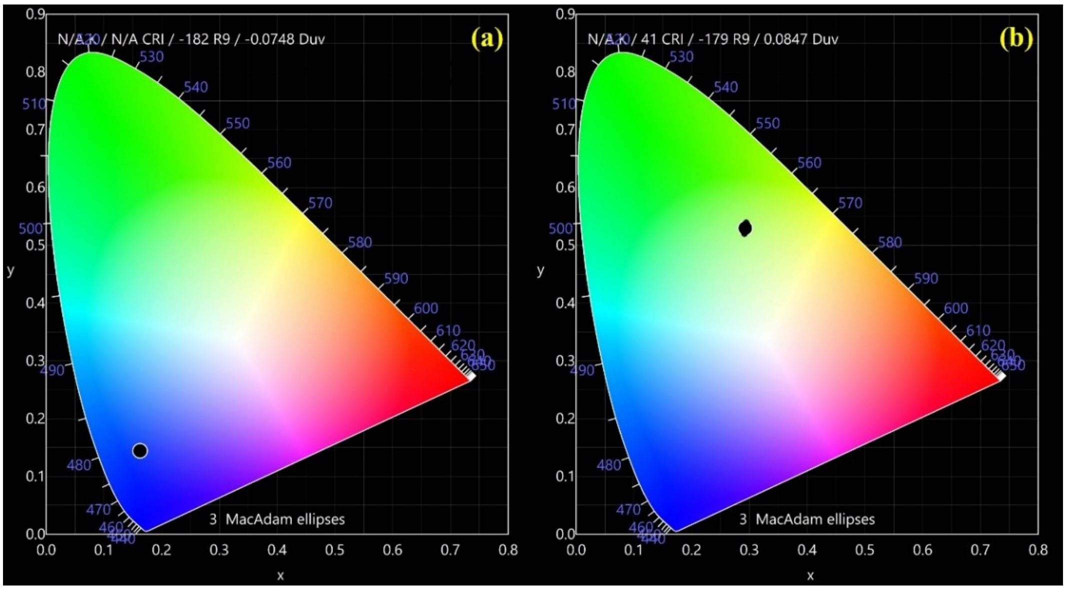

Figure S8. *CIE diagram of S-g-C_3N_4 before* ***(a)*** *and after* ***(b)*** *addition with known concentration (120 μM) of BIL during sensing.*

S9. Comparison PL spectrum of S-g-C_3N_4 before and after addition with BIL:

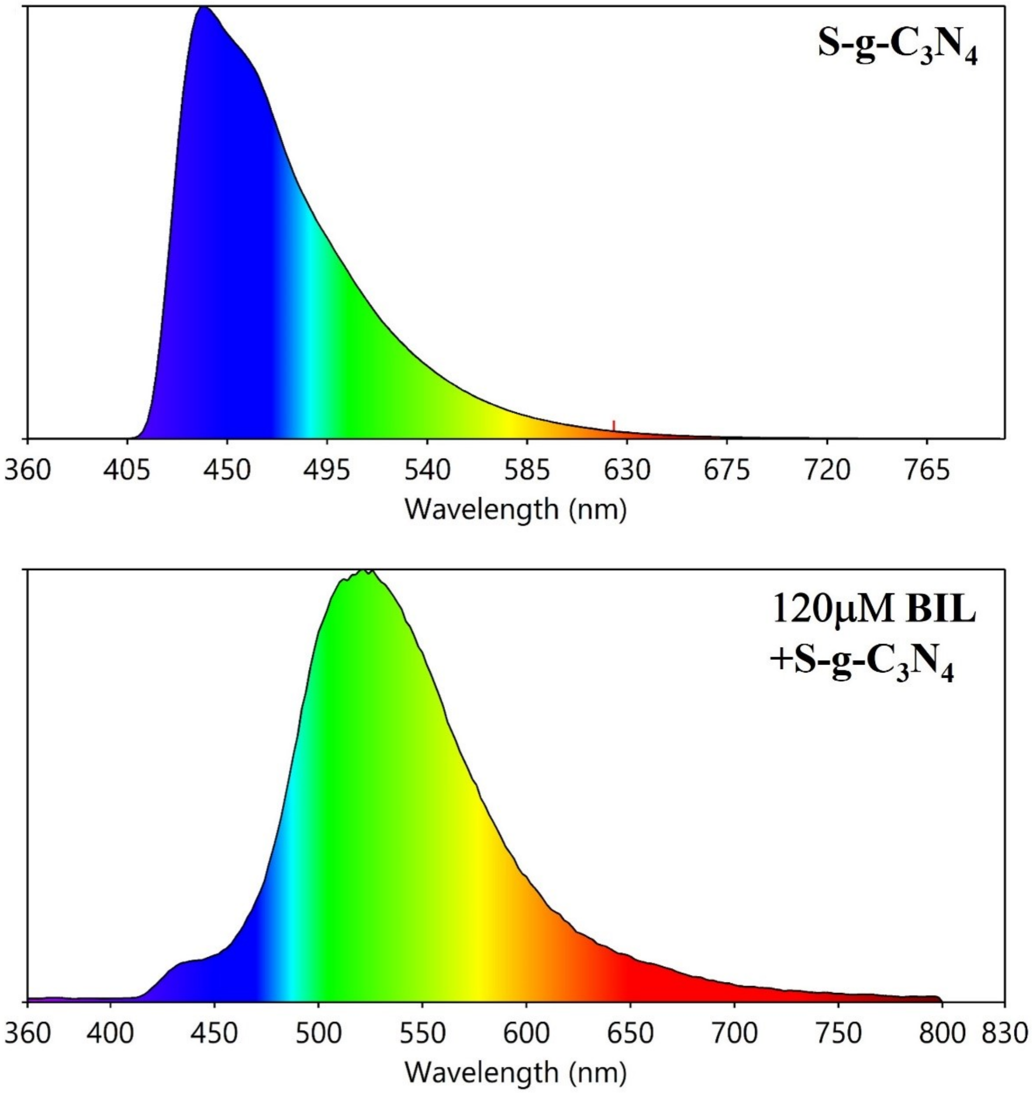

Figure S9. *PL Spectrum of S-g-C_3N_4 before* ***(a)*** *and after* ***(b)*** *addition with known concentration (120 µM) of BIL during sensing.*

S10.Mechanism behind quenching:

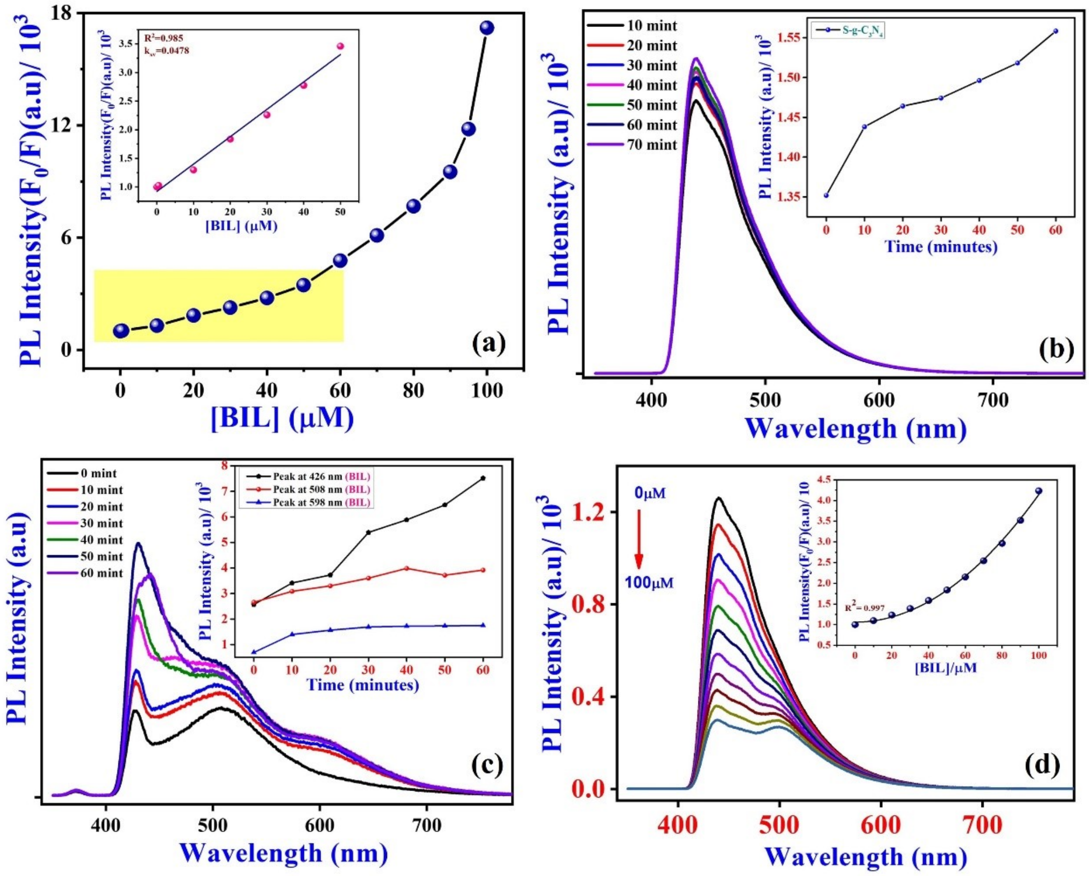

Figure S10.*(a) Stern Volmer quenching plot, Time dependent PL spectrum of S- g-C_3N_4 (b), and BIL (c) in 0.1 M PBS (pH =7.4). (d) PL Spectrum profile of S- g-C_3N_4 upon addition of 10 μM of BIL in high viscous ethylene glycol (viscosity method).*

S11. Zeta potential:

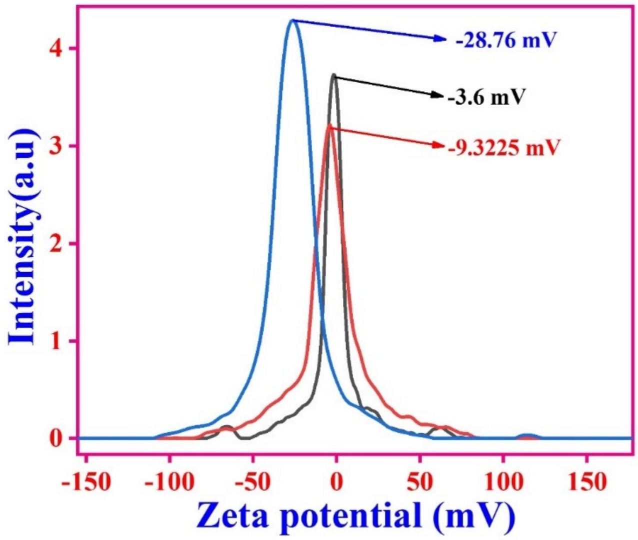

Figure S11. *Zeta potential profile of S-g-*C_3N_4 *(black), S-g-*C_3N4 *+10 µM of BIL (red), and S-g-*C_3N_4 *+0.15 mM of BIL (blue) respectively.*

S12. particle size distribution:

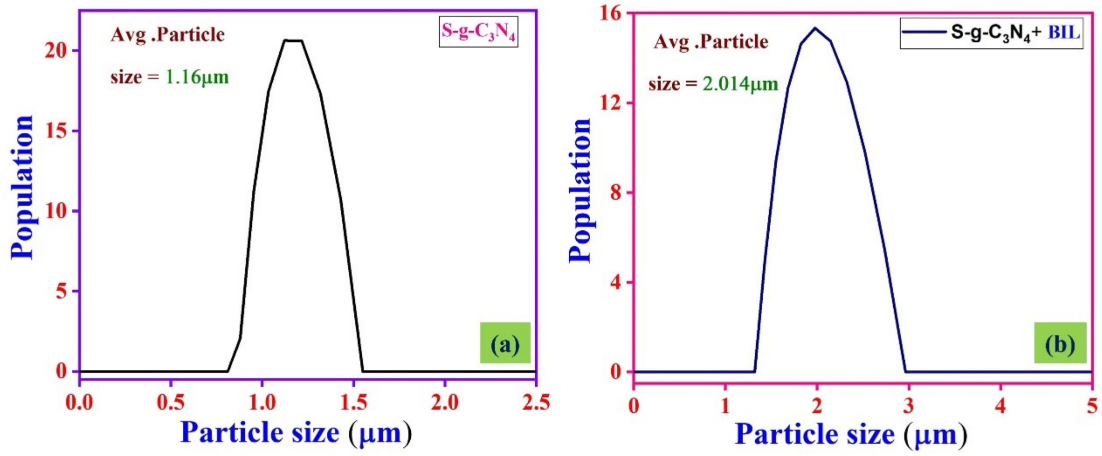

Figure S12. *The average particle size of S-g-C_3N_4 before* ***(a)*** *and after* ***(b)*** *addition of BIL.*

Section 4.Kinetics and Thermodynamic studies :

S13. Temperature dependence Stern Volmer plot:

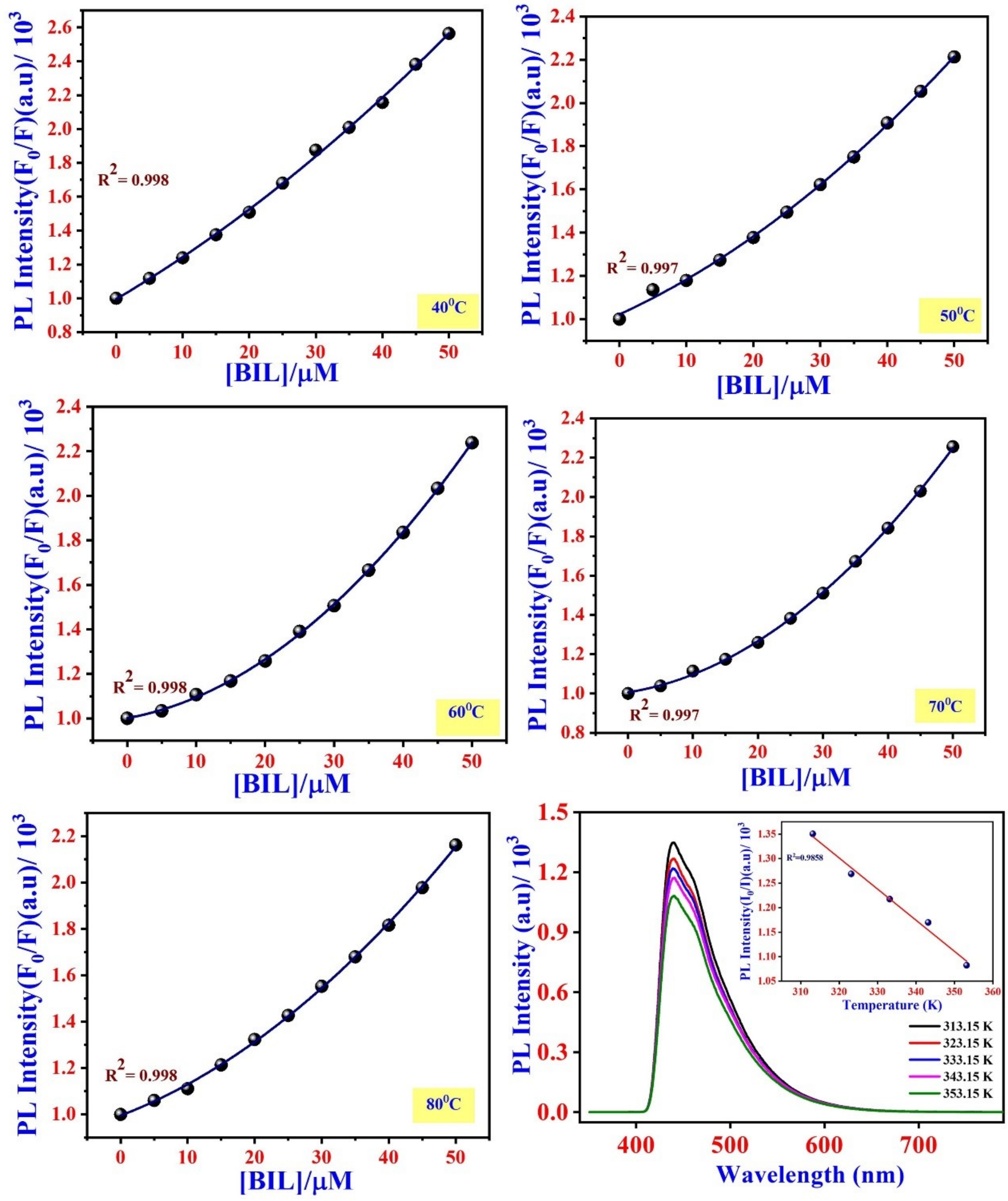

Figure S13. *A plot of concentration of BIL vs PL intensity of S-g-C_3N_4 (F_0-F) at various temperature (Temperature dependence Stern Volmer plot).*

S14. Temperature dependence modified Stern Volmer plot (Association plot):

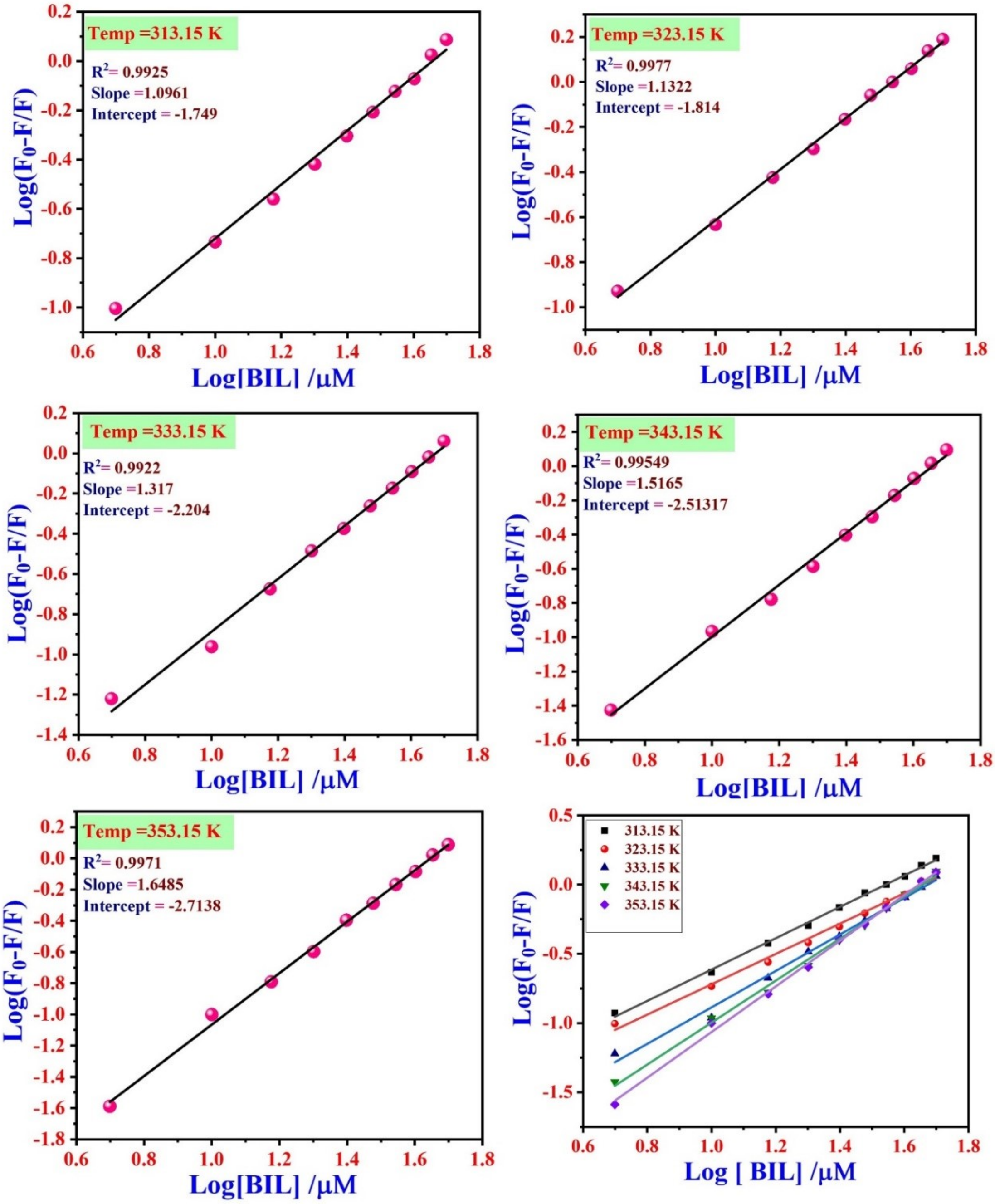

Figure S14. A plot of concentration of Log of BIL vs PL intensity of S-g-C_3N_4 Log of(F_0-F/F) at various temperature (Association plot).

S15. Confirmation of Hydrogen bond formation between S-g-C_3N_4 and bilirubin via FT-IR:

To understand the influence of possible binding of BIL with S-g-C_3N_4, FTIR spectra of S-g-C_3N_4 in the absence and presence of BIL were recorded as illustrated in Figure. 6. The analysis of S-g-C_3N_4 reveals a fascinating structure characterized by sp2-bonded features that are reminiscent of graphite.[3]The broad bands in the spectrum illustrate the stretching and deformation modes of the -NH_2 groups. Notably, the dynamic stretching vibrations of the tri-s-triazine ring were observed at 1242 cm^{-1}, 1328 cm^{-1}, and 1566 cm^{-1}, accompanied by bending vibrations at 811 cm^{-1}[4]. Key absorption peaks at 1406 cm^{-1} and 1635 cm^{-1} were attributed to C=N and C-N bonds, respectively[4]. In the case of BIL, bands observed at 3401 cm^{-1} and 3175 cm^{-1} were assigned to the stretching modes of pyrrole N–H and lactam N–H, respectively. Upon interaction with S-g-C_3N_4, the pyrrole N–H band shifted to 3446 cm^{-1} and broadened. The asymmetric lactam N–H stretching frequency of BIL appeared as a shoulder in the broad band of pyrrole N–H. The band at 1240 cm^{-1}, associated with a pyrrole ring breathing mode, was slightly broadened and potentially shifted to 1243 cm^{-1} due to surface interactions with S-g-C_3N_4.in the case of BIL, which contains two carboxyl side chains, produces a carboxyl stretching vibration at 1689 cm^{-1}, a band that is absent in bare S-g-C_3N_4 because of the lack of a carboxyl functional group. When bilirubin interacts with S-g-C_3N_4, the corresponding carboxyl stretching vibration is shifted. Additionally, two weaker bands at 1566 cm^{-1} and 1407 cm^{-1} were assigned to the asymmetric and symmetric stretching vibrations of the carboxylate form (COO-) of BIL, which shifts toward a higher wavenumber upon reaction with S-g-C_3N_4. The band at 1640 cm^{-1}, which corresponds to the lactam C=O vibration, was shifted to 1645 cm^{-1} when interacting with S-g-C_3N_4[5]. Other bands at 1240, 987, and 812 cm^{-1} from BIL were connected to the lactam systems (C–C, C–N vibrations) and exhibited slight broadening and shifts due to this interaction. Overall, the observed broadening of OH and NH stretches, as well as the changes in NH bending and C–O stretching frequencies, suggest the possibility of hydrogen bonding occurring between BIL and S-g-C_3N_4[6,7]

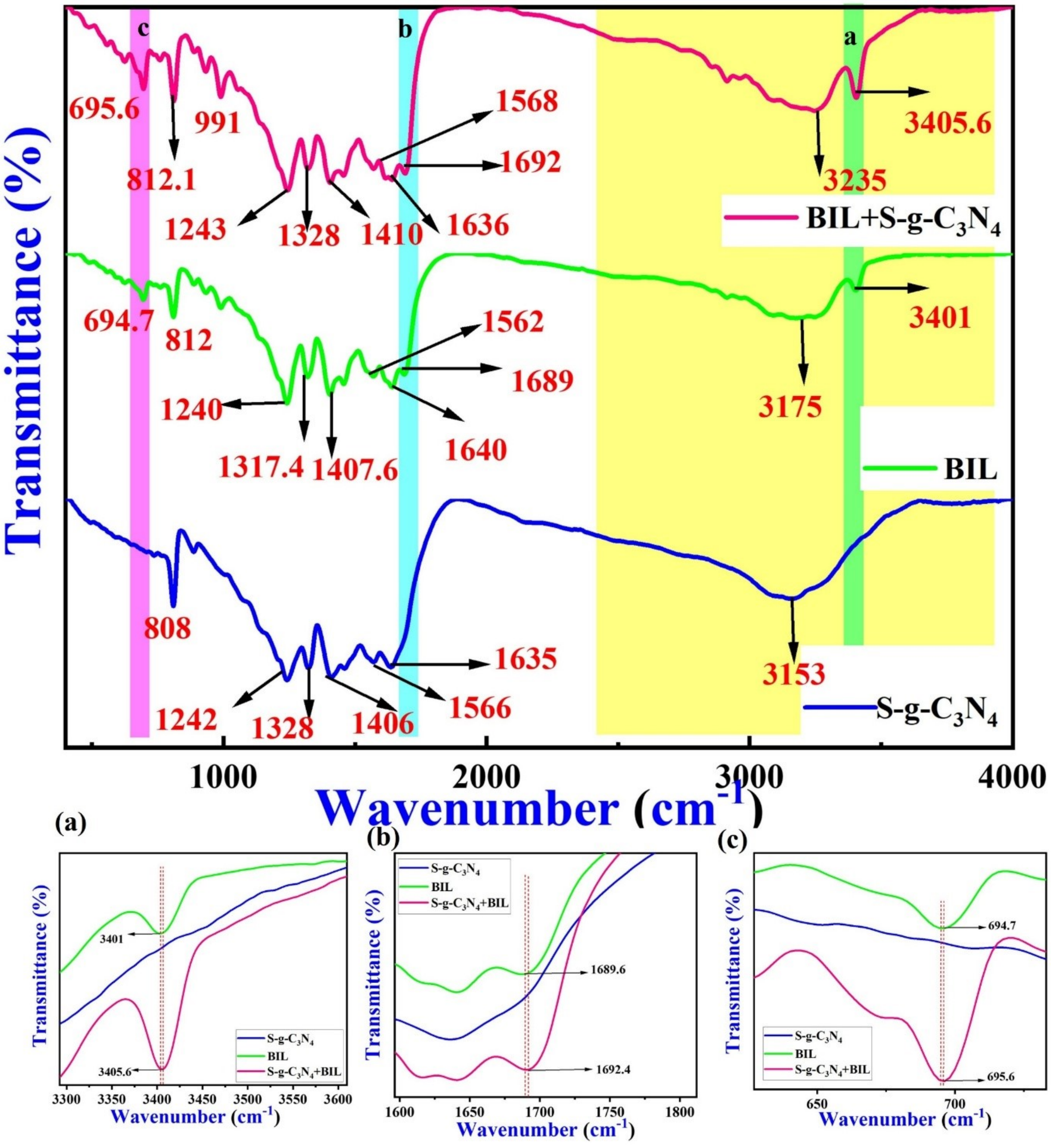

Figure S15. *comparative FT-IR profiles of bare S-g-C_3N_4* ***(blue),*** *Bare BIL* ***(green)*** *and the synergistic combination of both BIL and S-g-C_3N_4* ***(pink).***

Section 5. Interference studies

S16.Interference analysis.

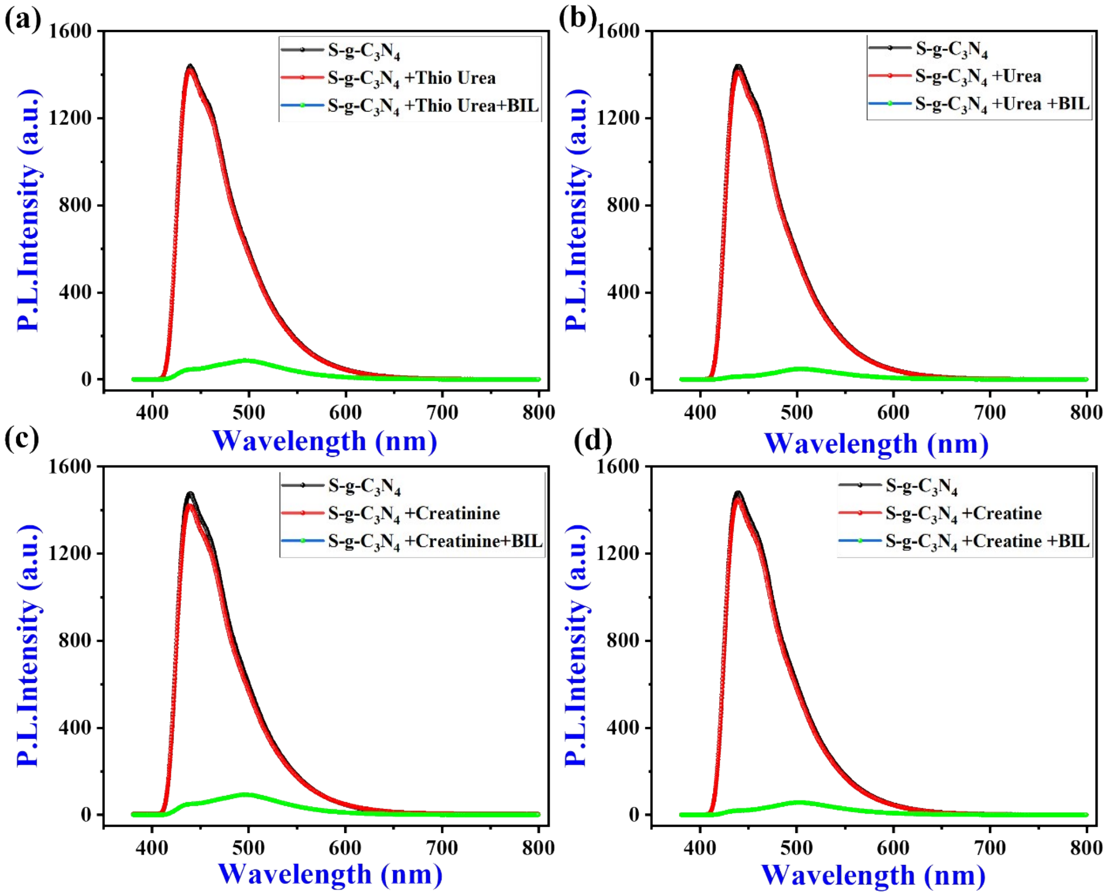

Figure S16. *Comparison PL spectrum of S-g-C_3N_4 with various interferences molecules* ***(a)*** *Thio Urea,* ***(b)*** *Urea,* ***(c)*** *Creatinine,* ***(d)*** *Creatine. (****Note:*** *concentration of analyte 0.1mM interference molecules 5mM.)*

S17.Interference analysis.

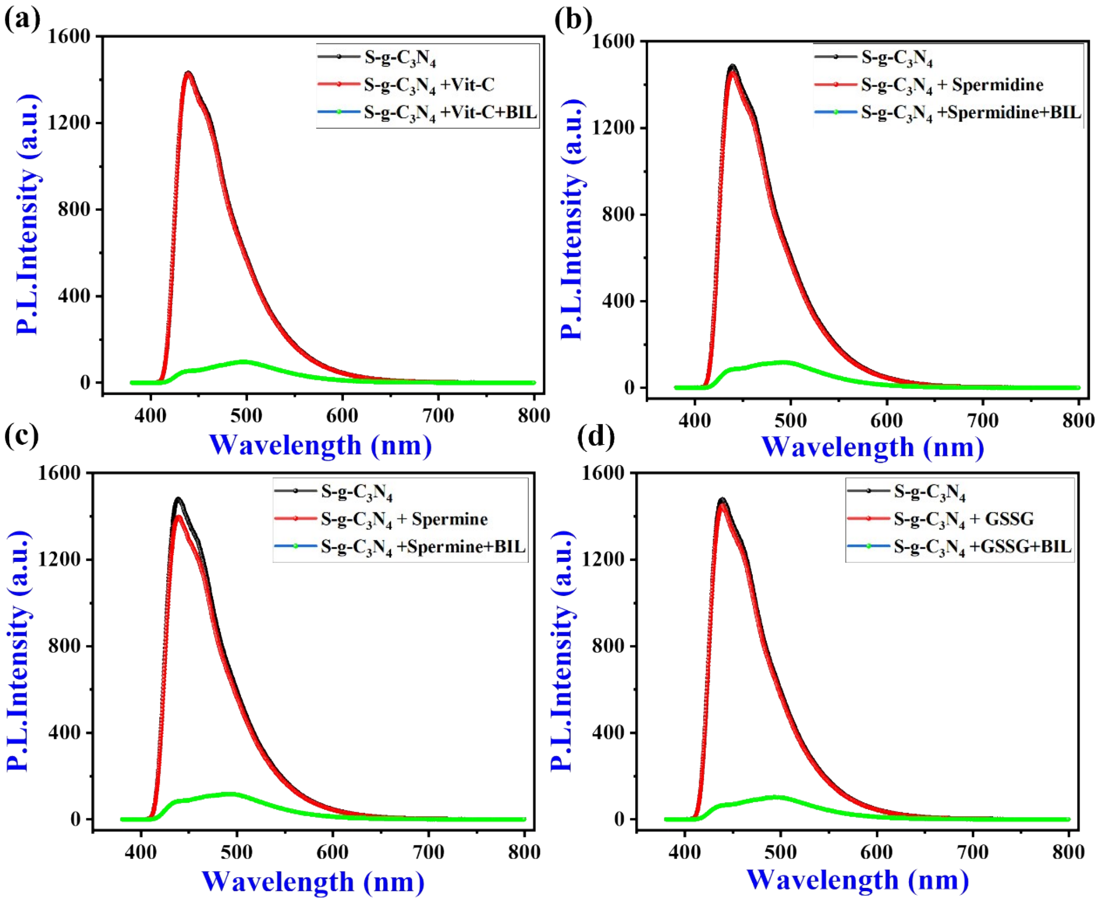

Figure S17. *Comparison PL spectrum of S-g-C_3N_4 with various interferences molecules* ***(a)*** *Vit-C,* ***(b)*** *Spermidine,* ***(c)*** *Spermine ,**(d)*** *GSSG. (**Note :*** *concentration of analyte 0.1mM interference molecules 5mM.)*

S18.Interference analysis.

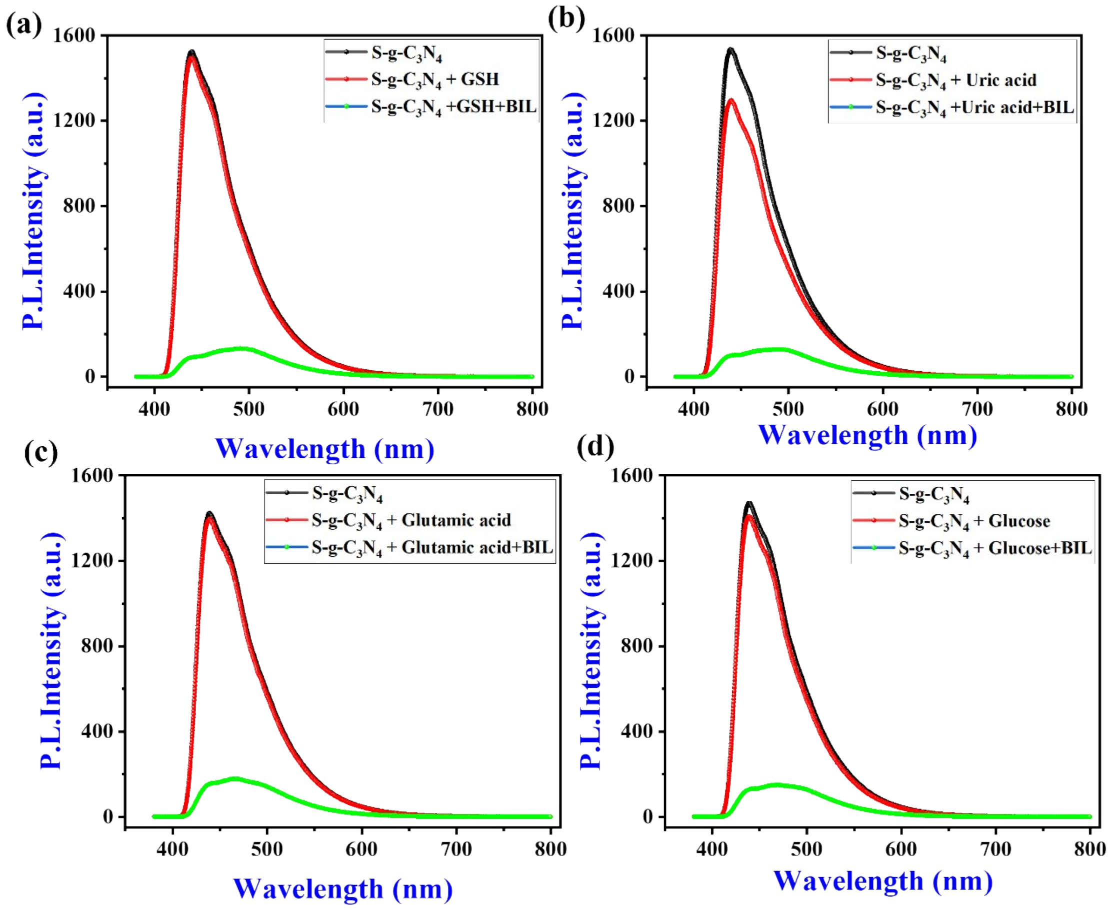

Figure S18. *Comparison PL spectrum of S-g-C_3N_4 with various interferences molecules* ***(a)*** *GSH,* ***(b)*** *Uric acid,* ***(c)*** *Glutamic acid,* ***(d)*** *Glucose. (**Note :** concentration of analyte 0.1mM interference molecules 5mM.)*

S19.Interference analysis:

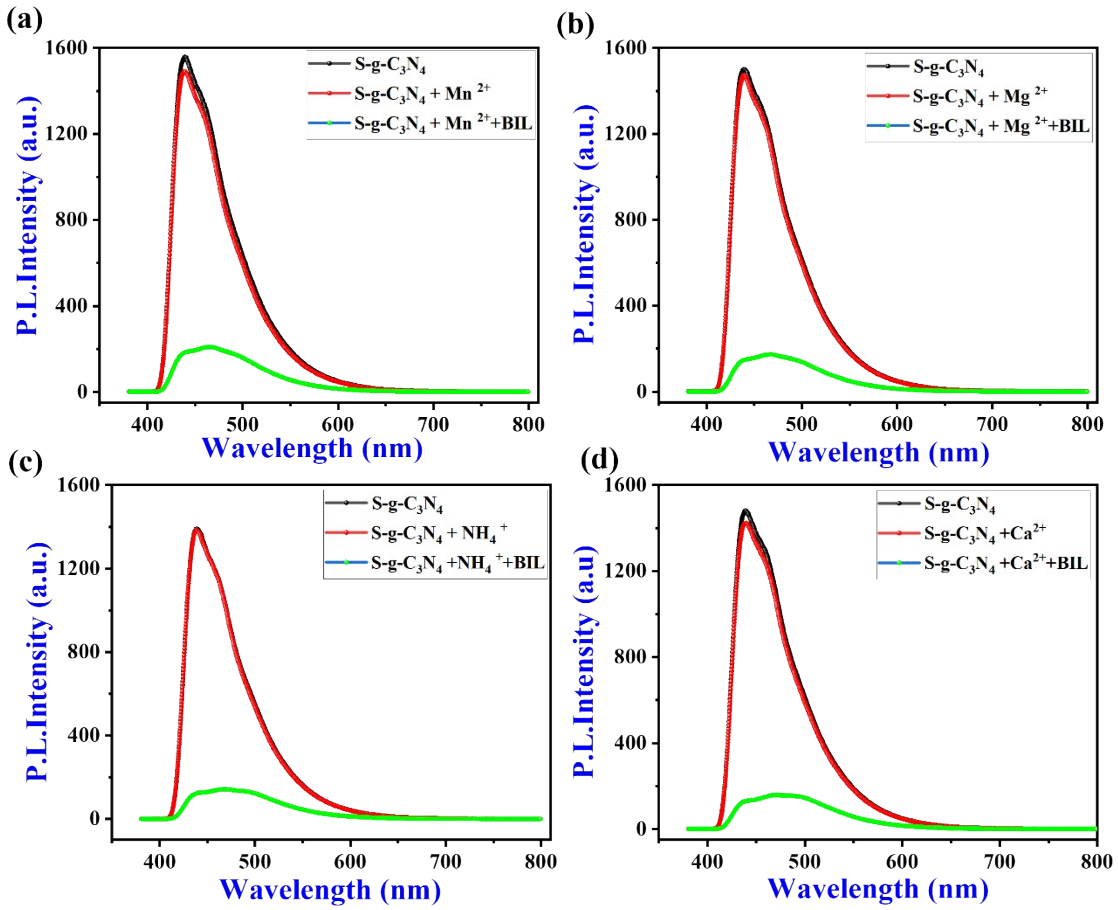

Figure S19. *Comparison PL spectrum of* $S\text{-}g\text{-}C_3N_4$ *with various interferences molecules* ***(a)*** *Manganese ions,* ***(b)*** *Magnesium ions,* ***(c)*** *ammonium ions,* ***(d)*** *Calcium ions. (****Note :*** *concentration of analyte 0.1mM interference molecules 5mM.)*

S20.Interference analysis:

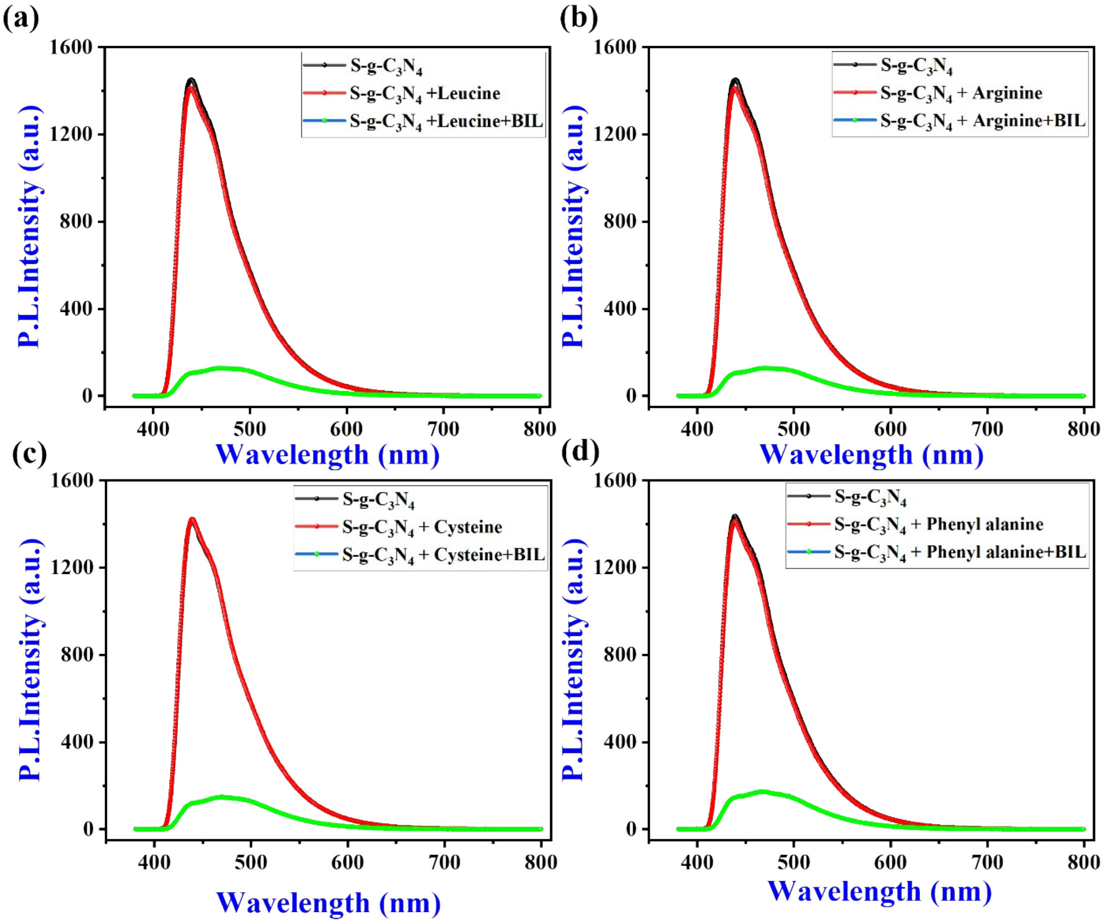

Figure S20. *Comparison PL spectrum of S-g-C_3N_4 with various interferences molecules* ***(a)*** *Leucine,* ***(b)*** *Arginine,* ***(c)*** *Cysteine,* ***(d)*** *phenyl alanine. (****Note :*** *concentration of analyte 0.1mM interference molecules 5mM.)*

S21.Interference analysis:

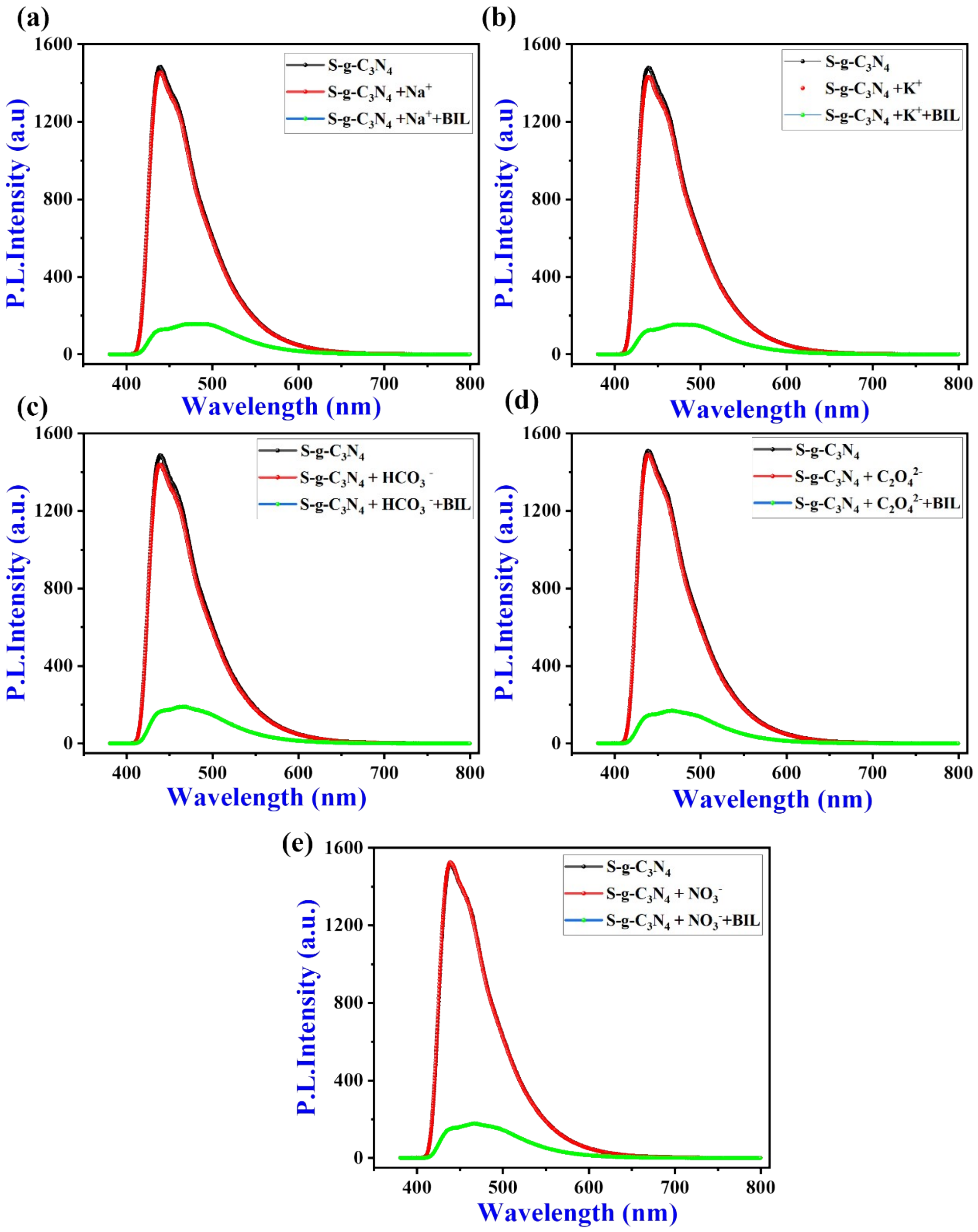

Figure S21. *Comparison PL spectrum of S-g-C_3N_4 with various interferences molecules* ***(a)*** *sodium ion,* ***(b)*** *potassium ion,* ***(c)*** *bicarbonate ions ,****(d)*** *oxalate ions ,****(e)*** *nitrate ions. (****Note :*** *concentration of analyte 0.1mM interference molecules 5mM.)*

Section 5. Real sample analysis .

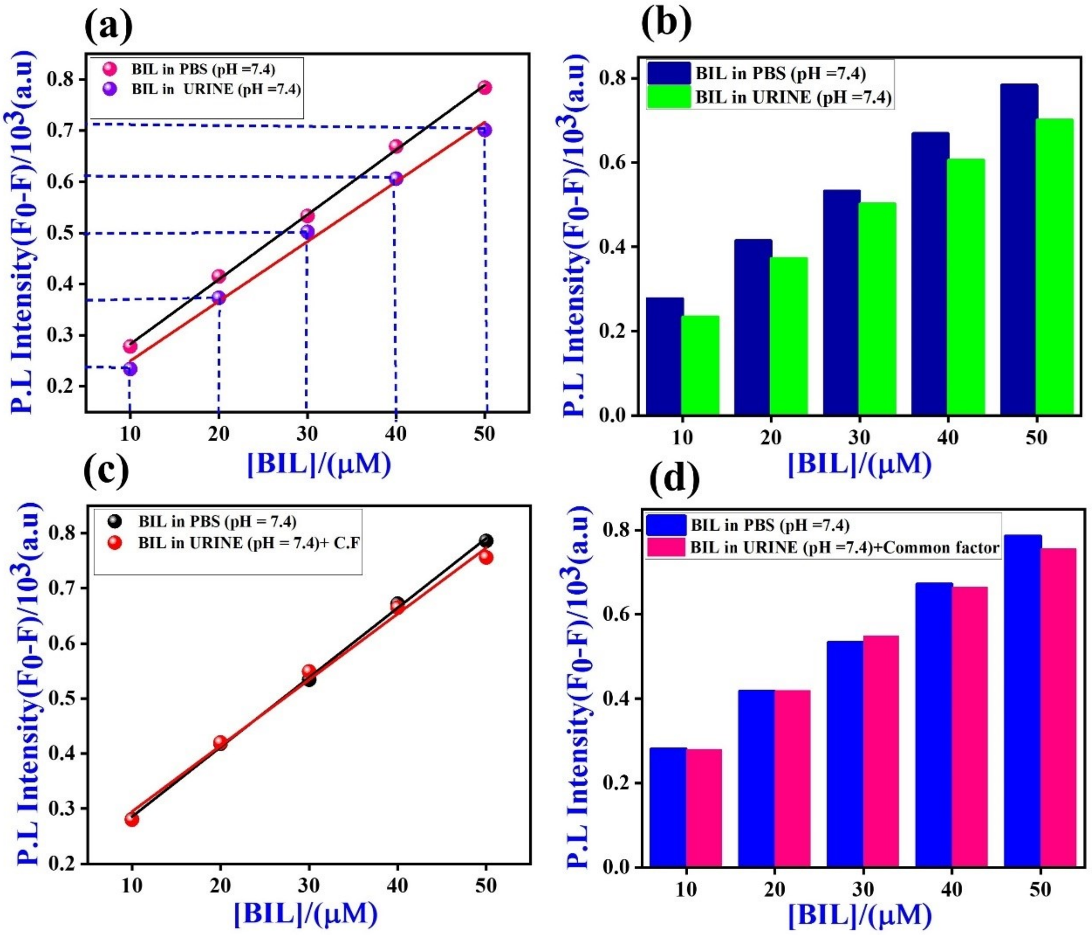

Figure S22. *(a) Comparison calibration Plot of PL intensity of fluorophore in 0.1M PBS (pH = 10) upon addition of Known concentration of spiked GSH in human urine.(b) their corresponding histogram. (a) Comparison calibration Plot of PL intensity of fluorophore in 0.1M PBS (pH = 10) upon addition of Known concentration of spiked GSH in human urine multiple with common factor .(d) their corresponding histogram.*

Table S1. Literature comparison

S. No	Fluorescent probe	Synthesis method	Fluorescence response	Linear range (µM)	LOD (µM)	Ref
1	O-Phenylene diamine and dopamine-based carbon dots	Solvo thermal method	Turn-off	0 -400	7.2	[8]
2	Gold nanocluster supported film on &polydopamine	Chemical method	Fluorescence-Turn-off	0.8 - 50	0.61	[9]
3	Blue emitting Graphene quantum dots	Solvo thermal method	Fluorescence-Turn-off	40.53 - 237.55	9	[10]
4	L-Cystine modified Mn ZnS QDs.	Microwave assisted wet chemical method	Fluorescence-Turn-off	10.99 - 63.84	1.8	[11]
5	L-Cystine modified Cu nano cluster	Solvo thermal method	Fluorescence-Turn-off	1-10	0.229	[12]
6	Eu(III) MOF	Chemical method	Fluorescence-Turn-off	0-56.6	1.75	[13]

7	Eu(III) post factionalized Zr(IV) MOF	Solvo thermal method	Fluorescence-Turn-off	0-15	0.45	[14]
8	Tb(III) post factionalized Zr(IV) MOF-808	Chemical method	Fluorescence-Turn-off	0.4-30	0.26	[15]
9	GSH-AuNCs@ZIF-8	Chemical method	Fluorescence-Turn-off	0-15	0.07	[16]
10	GSH-CuNCs	Chemical method	Fluorescence-Turn-off	0.8-9	0.148	[17]
11	**Blue emitting S-g-C_3N_4.**	**Greener Solvent free thermal polycondensation method**	**Fluorescence - Turn-off**	**0.04 - 80**	**0.00256**	**This work**

Kinetic parameters

Table S2. Temperature dependant stern Volmer quenching constant:

Calculation of Stern Volmer quenching constant (K_{sv}) from stern Volmer plot.

Temperature (kelvin)	**Stern volmer quenching constant (K_{sv}) X* 10^3 (L mol^{-1})**	**Intercept**
313.15	23.2	0.99572
323.15	14.19	1.022
333.15	11.01	1.00122
343.15	5.5	0.99523
353.15	4.14	1.006

Thermodynamic parameters:

Table S3. Calculation of thermodynamic parameters change in enthalpy, change in entropy, change in Gibbs free energy of a given thermodynamic system (quenching between BIL and S-g-C_3N_4. (From association plot).

Temperature (kelvin)	**Change in Enthalpy(ΔH) (KJ mol^{-1})**	**Change in Entropy(ΔS) (J mol^{-1} K^{-1})**	**Change in Gibbs free energy (ΔG) (KJ mol^{-1})**	**Co-relation coefficient (R^2)**
313.15	-40.194	-44.596	-26.229	0.9885
323.15			-25.790	
333.15			-25.337	

343.15	-24.891
353.15	-24.445

Table S4. Calculation of change in Gibbs free energy of a given thermodynamic system (By using the thermodynamic equation $(\Delta G) =- RTlnk$)

Temperature (kelvin)	**Stern volmer quenching constant (Ksv) X* 10^3 (L mol^{-1})**	**lnK**	**Change in Gibbs free energy (ΔG) (KJ mol^{-1})**	**Co-relation coefficient (R^2)**
313.15	23.2	10.043	-26.147	0.9976
323.15	14.19	9.5468	-25.649	0.9946
333.15	11.01	9.3056	-25.774	0.9952
343.15	5.5	8.6125	-24.571	0.9958
353.15	4.14	8.3247	-24.442	0.9985

Table S5. Calculation of binding site no and binding constant, of a given thermodynamic system (quenching between BIL and S-g-C_3N_4.) (From association plot).

Temperature (kelvin)	**Binding constant (K) X* 10^3**	**Binding site no (n)**	**Co-relation coefficient (R^2)**
313.15	18	1.0961	0.9976
323.15	15	1.1322	0.9951
333.15	6.2	1.317	0.9979
343.15	3	1.51	0.9986
353.15	1.9	1.648	0.9953

References:

(1) Sarigul, N.; Korkmaz, F.; Kurultak, İ. A New Artificial Urine Protocol to Better Imitate Human Urine. *Sci Rep* **2019**, *9* (1). https://doi.org/10.1038/s41598-019-56693-4.

(2) Dong, L.; Chu, H.; Xu, S.; Li, Y.; Zhao, S.; Li, D. Band Structure Tuning of G-C3N4via Sulfur Doping for Broadband near-Infrared Ultrafast Photonic Applications. *Nanophotonics* **2022**, *11* (1), 139–151. https://doi.org/10.1515/nanoph-2021-0549.

(3) Rajkumar, C.; Veerakumar, P.; Chen, S. M.; Thirumalraj, B.; Lin, K. C. Ultrathin Sulfur-Doped Graphitic Carbon Nitride Nanosheets As Metal-Free Catalyst for Electrochemical Sensing and Catalytic Removal of 4-Nitrophenol. *ACS Sustain Chem Eng* **2018**, *6* (12), 16021–16031. https://doi.org/10.1021/acssuschemeng.8b02041.

(4) Wang, K.; Li, Q.; Liu, B.; Cheng, B.; Ho, W.; Yu, J. Sulfur-Doped g-C3N4 with Enhanced Photocatalytic CO2-Reduction Performance. *Appl Catal B* **2015**, *176–177*, 44–52. https://doi.org/10.1016/j.apcatb.2015.03.045.

(5) Karmakar, S.; Kanti Das, T.; Saha, A. Ultra-Low Level Detection of Biomarker Bilirubin by Graphene Quantum Dots and Bovine Serum Albumin Enabled Turn-on Sensing. *Microchemical Journal* **2024**, *204*. https://doi.org/10.1016/j.microc.2024.111045.

(6) Patel, M. R.; Chetti, P.; Park, T. J.; Kailasa, S. K. Fluorescence Sensing of Bilirubin Using Water-Stable Ethylenediaminetetraacetic Acid-Functionalized CsPbBr3 Perovskite Quantum Dots. *ACS Appl Nano Mater* **2024**. https://doi.org/10.1021/acsanm.4c03489.

(7) Karmakar, S.; Kanti Das, T.; Saha, A. Ultra-Low Level Detection of Biomarker Bilirubin by Graphene Quantum Dots and Bovine Serum Albumin Enabled Turn-on Sensing. *Microchemical Journal* **2024**, *204*. https://doi.org/10.1016/j.microc.2024.111045.

(8) Bao, L.; Liu, S. A Dual-Emission Polymer Carbon Nanoparticles for Ratiometric and Visual Detection of PH Value and Bilirubin. *Spectrochim Acta A Mol Biomol Spectrosc* **2022**, *267*, 120513. https://doi.org/10.1016/J.SAA.2021.120513.

(9) Li, Z.; Xiao, W.; Huang, R.; Shi, Y.; Fang, C.; Chen, Z. A Gold Nanoclusters Film Supported on Polydopamine for Fluorescent Sensing of Free Bilirubin. *Sensors (Switzerland)* **2019**, *19* (7). https://doi.org/10.3390/s19071726.

(10) Kumar, H.; Obrai, S. Highly Sensitive and Selective Detection of Free Bilirubin Using Blue Emitting Graphene Quantum Dots (GQDs). https://doi.org/10.1007/s12039-022.

(11) Abha, K.; Nebu, J.; Anjali Devi, J. S.; Aparna, R. S.; Anjana, R. R.; Aswathy, A. O.; George, S. Photoluminescence Sensing of Bilirubin in Human Serum Using L-Cysteine Tailored Manganese Doped Zinc Sulphide Quantum Dots. *Sens Actuators B Chem* **2019**, *282*, 300–308. https://doi.org/10.1016/j.snb.2018.11.063.

(12) Anand, S. K.; Mathew, M. R.; Kumar, K. G. A Simple and Cost Effective Turn off Fluorescence Sensor for Biliverdin and Bilirubin Based on L-Cysteine Modulated Copper Nanoclusters. *J Fluoresc* **2020**, *30* (1), 63–70. https://doi.org/10.1007/s10895-019-02470-5.

(13) Xu, P.; Yang, H. W.; Shi, J. L.; Ding, B.; Zhao, X. J.; Yang, E. C. Efficient Detection of a Biomarker for Infant Jaundice by a Europium(Iii)-Organic Framework Luminescence Sensor. *RSC Adv* **2019**, *9* (64), 37584–37593. https://doi.org/10.1039/c9ra08604h.

(14) Xia, C.; Xu, Y.; Cao, M. M.; Liu, Y. P.; Xia, J. F.; Jiang, D. Y.; Zhou, G. H.; Xie, R. J.; Zhang, D. F.; Li, H. L. A Selective and Sensitive Fluorescent Probe for Bilirubin in Human Serum Based on Europium(III) Post-Functionalized Zr(IV)-Based MOFs. *Talanta* **2020**, *212*. https://doi.org/10.1016/j.talanta.2020.120795.

(15) Yi, K.; Li, H.; Zhang, X.; Zhang, L. Designed Tb(III)-Functionalized MOF-808 as Visible Fluorescent Probes for Monitoring Bilirubin and Identifying Fingerprints. *Inorg Chem* **2021**, *60* (5), 3172–3180. https://doi.org/10.1021/acs.inorgchem.0c03312.

(16) Xia, M.; Sui, Y.; Guo, Y.; Zhang, Y. Aggregation-Induced Emission Enhancement of Gold Nanoclusters in Metal-Organic Frameworks for Highly Sensitive Fluorescent Detection of Bilirubin. *Analyst* **2021**, *146* (3), 904–910. https://doi.org/10.1039/d0an02076a.

(17) Anand, S. K.; Mathew, M. R.; Girish Kumar, K. A Dual Channel Optical Sensor for Biliverdin and Bilirubin Using Glutathione Capped Copper Nanoclusters. *J Photochem Photobiol A Chem* **2021**, *418*. https://doi.org/10.1016/j.jphotochem.2021.113379.